Virtual histology of the human heart using optical coherence tomography

Christina M. Ambrosi
Washington University in St. Louis
Department of Biomedical Engineering
1 Brookings Drive
Campus Box 1097
St. Louis, Missouri 63130

Nader Moazami
Washington University
School of Medicine
Division of Cardiothoracic Surgery
600 South Euclid Avenue
St. Louis, Missouri 63110

Andrew M. Rollins
Case Western Reserve University
Department of Biomedical Engineering
10900 Euclid Avenue
Cleveland, Ohio 44106

Igor R. Efimov
Washington University in St. Louis
Department of Biomedical Engineering
1 Brookings Drive
Campus Box 1097
St. Louis, Missouri 63130

Abstract. Optical coherence tomography (OCT) allows for the visualization of micron-scale structures within nontransparent biological tissues. For the first time, we demonstrate the use of OCT in identifying components of the cardiac conduction system and other structures in the explanted human heart. Reconstructions of cardiac structures up to 2 mm below the tissue surface were achieved and validated with Masson Trichrome histology in atrial, ventricular, sinoatrial nodal, and atrioventricular nodal preparations. The high spatial resolution of OCT provides visualization of cardiac fibers within the myocardium, as well as elements of the cardiac conduction system; however, a limiting factor remains its depth penetration, demonstrated to be ~2 mm in cardiac tissues. Despite its currently limited imaging depth, the use of OCT to identify the structural determinants of both normal and abnormal function in the intact human heart is critical in its development as a potential aid to intracardiac arrhythmia diagnosis and therapy.
[DOI: 10.1117/1.3213604]

Keywords: biomedical optics; medical imaging; coherence; tomography; structure; myocardium.

Paper 09084R received Mar. 12, 2009; revised manuscript received Jun. 26, 2009; accepted for publication Jul. 6, 2009; published online Sep. 8, 2009.

1 Introduction

In the 17 years since its initial introduction,[1] optical coherence tomography (OCT) has gained prominence as a diagnostic imaging modality in the fields of ophthalmology,[2–4] vascular cardiology,[5–8] and dermatology.[9,10] Major clinical applications of cardiac OCT currently focus on the visualization of the coronary vasculature—for example, identifying unstable plaques and guiding interventional techniques such as stent placement.[7] However, within the realms of cardiac research, the applications of OCT have been steadily increasing. Recently, OCT has been used to study developing murine and avian hearts,[11,12] as well as the morphogenesis and myocardial strains of the embryonic chick heart.[13] Additional studies have shown the utility of OCT in recognizing components of the cardiac conduction system of the rabbit, specifically the atrioventricular (AV) node[14] and the Purkinje network.[15] Our recent study extended these findings by exploring the relationship in the rabbit heart between function, visualized through optical mapping, and structure, imaged through OCT.[16] Concurrently, tools are also under development to analyze OCT data, including 3-D cardiac fiber structure.[17] In this study, we aimed to explore the utility of OCT in identifying components of the conduction system and other structures in the explanted human heart.

Clinical cardiac anatomical visualization and reconstruction techniques, including magnetic resonance imaging (MRI), computed tomography (CT), and ultrasound, have a variety of diagnostic capabilities, including localization of arterial plaques, evaluation of bypass grafts and stents, and quantification of wall properties. Although these modalities provide better depth of penetration than OCT, they deliver relatively low resolution images. In biological specimens, OCT, on the other hand, boasts spatial image resolutions ranging from submicrometer through 15 μm, which can be 10 to 100 times greater than other modalities and comparable to conventional histological analyses.[18,19]

In addition to its high spatial resolution, OCT also has other advantages pertaining to diagnostics and surgical guidance. First, OCT can be performed in real time and *in situ*, allowing for convenient online guidance and evaluation of treatment. Second, OCT technology can be miniaturized to a catheter-based imaging system[20,21] and threaded through the vasculature into the cardiac chambers. Last, OCT can be used for Doppler blood flow and the quantification of blood oxygenation.[22,23]

Despite its high spatial resolution, OCT is limited by its depth penetration, estimated to be 2 to 3 mm in nontransparent biological tissues.[19] Although there are techniques in development to enhance both its depth penetration and resolution,[19,24,25] currently standard OCT does not achieve the

Address all correspondence to: Igor R. Efimov, Washington University in St. Louis, 1 Brookings Drive, Campus Box 1097, St. Louis, MO 63130. Tel: (314) 935-8612; Fax: (314) 935-8377; E-mail: igor@wustl.edu

1083-3668/2009/14(5)/054002/7/$25.00 © 2009 SPIE

Table 1 Clinical data. Relevant clinical information regarding each specimen. The mean age of the patients was 50±10 years.

Heart number	Gender	Age	Diagnosis
1	Male	58	Intercerebral injury
2	Male	46	Ischemic cardiomyopathy
3	Female	37	Idiopathic cardiomyopathy
4	Female	52	Nonischemic cardiomyopathy
5	Female	45	Hypertrophic obstructive cardiomyopathy
6	Male	55	Ischemic cardiomyopathy
7	Male	51	Ischemic cardiomyopathy
8	Male	60	Ischemic cardiomyopathy
9	Female	59	Idiopathic cardiomyopathy
10	Male	64	Nonischemic cardiomyopathy
11	Male	50	Ischemic cardiomyopathy
12	Male	48	Dilated cardiomyopathy
13	Male	28	Idiopathic cardiomyopathy

typical depths of MRI, CT, and ultrasound, which can acquire images of internal structures noninvasively. The advantage of OCT, however, lies in its superior spatial resolution, which enables the visualization of complex fiber architecture, as explored in this study of the explanted human heart.

2 Methods

2.1 *OCT Imaging*

The use of human hearts for research was approved by the Institutional Review Boards at both Washington University and the University of Minnesota.

Explanted failing human hearts ($n=12$) were obtained at the time of cardiac transplantation (Barnes-Jewish Hospital, St. Louis, Missouri) and immediately perfused with cardioplegic solution (4 °C). Tissue preparations from the right atria (RA), left ventricle (LV), infarcted right ventricle (RV), and atrioventricular junction (AVJ) were isolated from the rest of the heart. An additional sinoatrial nodal (SAN) specimen was obtained through the Upper Midwest Organ Procurement Organization (Life Source, St. Paul, Minnesota) and the University of Minnesota and shipped frozen to St. Louis. The tissues were perfused and fixed with 3.7% formaldehyde overnight and then transferred to 20% sucrose for 2 days. The tissues were photographed and clearly marked with pins to precisely correlate the OCT images with histology. OCT was performed 3 to 4 days later. Table 1 shows the clinical data regarding each specimen.

OCT, based on the principle of low-coherence interferometry, measures the backscatter of light. The coherence of the backscattered light from the sample arm (or tissue) and reference arm result in the generation of multiple A-scans (axial scans), which are then converted to pixel intensity and combined to form a tomogram (B-scan), or slice of tissue[26] (Fig. 1). The basics of our OCT system have been described previously.[16,27] We imaged all cardiac tissues in 1×1, 2×2, or 4.5×4.5 mm overlapping segments from the epicardial, endocardial, or transmural surfaces, with final axial and lateral resolutions of 10 μm (in air).

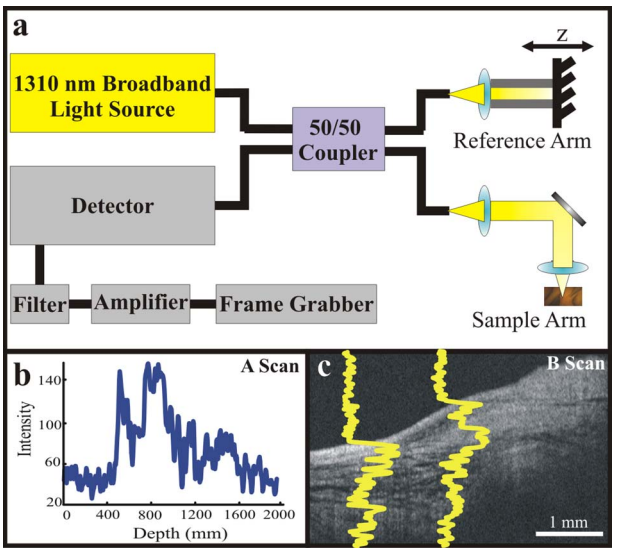

Fig. 1 Principles of OCT. (a) The setup for our benchtop OCT system includes a light source feeding directly into a 50/50 coupler splitting light between the reference and sample arms. The reflected light is then sensed by the detector, filtered, and amplified before advancing to the frame grabber. (b) An example A-scan describing the intensity of the reflected light at various depths in the tissue. (c) Multiple A-scans create the final image slice, or 2-D tomogram (B-scan).

2.2 *Histology*

After imaging, the tissue specimens were embedded and frozen in Tissue-Tek OCT compound (Electron Microscopy Sciences, Hatfield, Pennsylvania) and stored at −80 °C. The tissues were then cryosectioned at 16 μm, mounted on Superfrost Plus glass slides (Fisher Scientific). Sections were then stained using Masson Trichrome (IMEB, San Marcos, California) and visually compared with the corresponding OCT images.

2.3 *Computational Analysis and Statistics*

Images were processed using MATLAB (Mathworks) and Volocity (Improvision). Initially, each 2-D slice was acquired six times, and the six frames were then averaged together to reduce background noise. Subsequently, during post acquisition data analysis, median filtering was performed with a 3×3 smoothing kernel to reduce speckle noise.[28] Three-dimensional (3-D) tissue reconstructions were created using both Volocity and custom-written MATLAB programs. Additional analysis programs were developed in MATLAB for optical tissue slicing, to determine fiber orientation in relation to the tissue surface,[16] and for determination of the depth of OCT penetration. Depth penetration of each 4.5×4.5 mm field of view acquired across all tissue preparations was as-

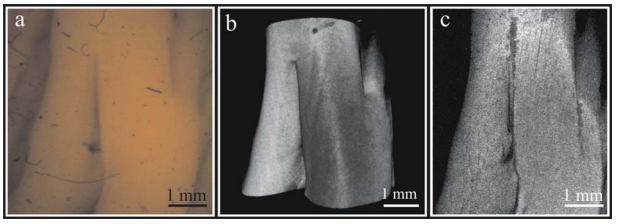

Fig. 2 OCT of the atria. (a) Atrial trabeculations of the RA appendage as viewed from the endocardium. (b) 3-D OCT rendering of the trabeculations. (c) Fiber architecture located 0.44 mm below the surface.

sessed via a global thresholding approach.[26] Quantitative data are expressed as mean ± standard deviation. A Student's *t*-test was used to determine statistical significance. A p value of <0.05 was considered statistically significant.

3 Results

3.1 *OCT of the Atria and Ventricles*

Atrial ($n=6$) and ventricular ($n=8$) preparations were imaged from both the endocardial and epicardial surfaces. Atrial depth penetration (0.94 ± 0.14 mm) significantly differed ($p = 1.74 \times 10^{-8}$) from that of the ventricles (1.29 ± 0.46 mm).

In atrial tissues, we created 3-D reconstructions of the trabeculations and distinguished fiber structures up to 1 mm below the endocardial surface (Fig. 2). In the ventricles, we were able to distinguish changes in fiber orientation in areas located within 4.5 mm of each other and 0.4 mm below the epicardial tissue surface [Figs. 3(a)–3(c)]. Although our current means of imaging does not achieve the depth required to reconstruct fiber architecture throughout the entire thickness of the human myocardium, we do have evidence that this can be accomplished in animal models, in which our current OCT system is able to penetrate through a larger percentage of the myocardium.[16]

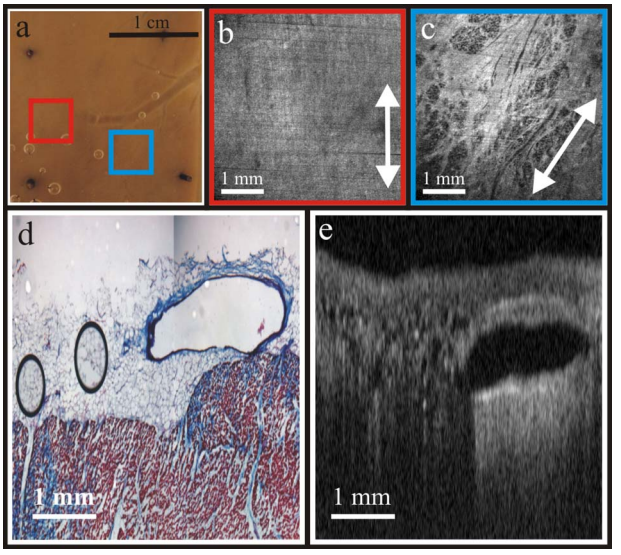

Fig. 3 OCT of the ventricles. (a) Photograph of an LV preparation as viewed from the epicardium. (b) Fiber architecture in the area indicated by the red box, 0.4 mm below the epicardial surface. (c) Fiber architecture 0.4 mm below the epicardial surface located 4.5 mm to the right of (b) as indicated by the blue box. The average angle of the fibers shifted by 30 deg. (d) Histologic cross section of the LV, affording a view of a coronary vein. (e) 2-D OCT image corresponding to (d). (Color online only.)

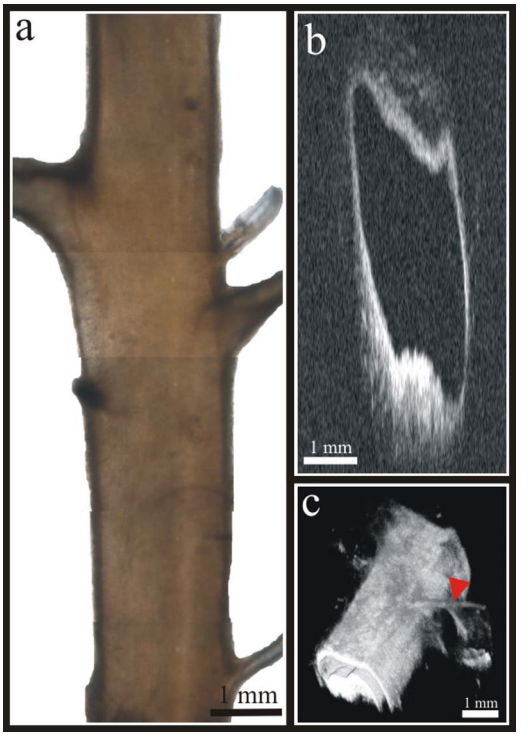

Fig. 4 OCT of an isolated coronary artery. (a) Photograph of an isolated coronary artery. (b) 2-D cross section of the artery. (c) 3-D OCT rendering of the artery. The red arrowhead indicates an arterial branch less than 1 mm in diameter. (Color online only.)

Epicardial OCT can also afford us a view of the coronary vessels. Figure 3(d) shows a histological cross section through an intact LV coronary vein, with the corresponding OCT cross section shown in Fig. 3(e). Figure 4 shows the resultant 2-D and 3-D OCT images from a coronary artery, isolated from the RV epicardial surface, with a main branch diameter of 2 mm. In particular, note that in Fig. 4(c), we are able to distinguish arterial branches less than 1 mm in diameter, as indicated by the arrowhead.

In addition, we imaged RV infarcts ($n=3$) epicardially, endocardially, and transmurally. Although we were able to detect significant ($p = 3.16 \times 10^{-7}$) changes in depth penetration as compared with adjacent noninfarcted ventricles, as measured from the epicardium and endocardium, we could not visually identify the fibroses from these surfaces with our OCT system. In contrast, when we imaged from the dissected transmural surface, as shown in Fig. 5, the fibrotic tissue of the infarct is clearly visible using OCT and correlates well with histology.

3.2 *OCT of the SAN*

OCT of the SAN was initially attempted from the endocardial surface, the primary point of access during intracardiac procedures. The SAN specimen was dissected to include the RA appendage, crista terminalis (CT), and approximately 2 cm of

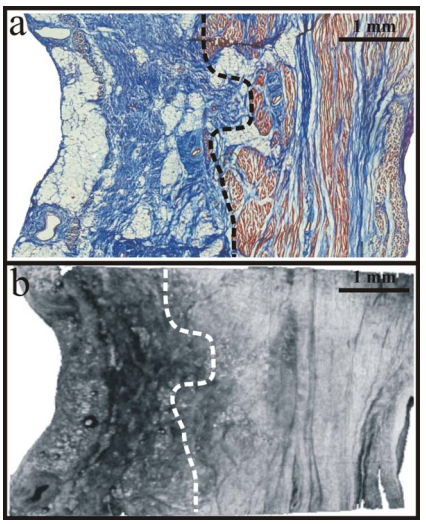

Fig. 5 Transmural OCT of the infarcted RV. (a) Histology of an epicardial RV infarct and its underlying tissue. (b) Corresponding OCT cross section of the infarct. The dotted line represents the approximate border between the infarct and viable myocardium.

atrium beyond the CT [Fig. 6(a)]. The specimen was then imaged in overlapping 4.5×4.5 mm segments, beginning along the CT and extending to the border of dissection. Figure 6(b) shows 3-D reconstructions of the tissue re-created from scans along the CT/RA border, as indicated by the dashed line in Fig. 6(a). Compared with the 2-D tomogram in Fig. 6(c), Fig. 6(d) exhibits an increased number of tissue layers as the transitional area closer to the SAN is approached. As the OCT field of view begins to incorporate the tissue layers above the SAN [Figs. 6(e) and 6(f)], it is readily apparent that the primary pacemaker of the heart, defined as a subepicardial structure,[29] is located too deep within the myocardium (at 1.75 mm) for imaging from the endocardial surface. The average depth penetration for this specimen from the endocardial surface was 1.06 ± 0.21 mm. Imaging from the epicardial surface was hindered by a layer of fat along the *sulcus terminalis*. Although fat intrinsically has a lower backscattered reflectance than normal cardiac tissue,[30] the loss in depth penetration was such that we could not visualize the SAN. In addition, the thin layer of epicardial fibrous tissue indicated by the arrow in Fig. 7(a) may contribute to the loss of depth when the SAN is imaged from the epicardium.

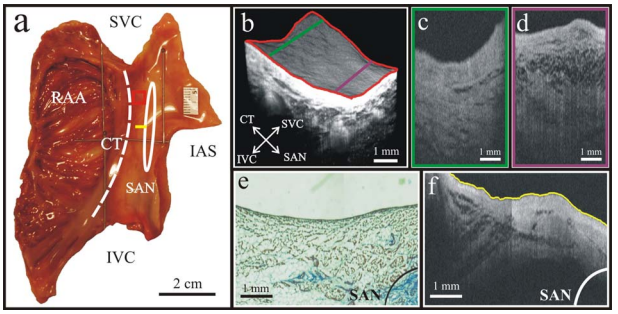

Fig. 6 Endocardial OCT of the SAN. (a) Dissected SAN preparation. (b) 3-D reconstruction of the tissue area as indicated by the red box. (c) and (d) 2-D tomograms from (b) as indicated by the green and purple lines. (e) Histology with the SAN indicated by the solid line in the lower-right corner. (f) OCT cross section corresponding to (e) showing a strong relationship between the transitional area as defined histologically and via OCT; however, the SAN is unable to be imaged endocardially using this method. Abbreviations—RAA: RA appendage; SVC: superior vena cava; IVC: inferior vena cava; CT: crista terminalis; IAS: interatrial septum; SAN: sinoatrial node. (Color online only.)

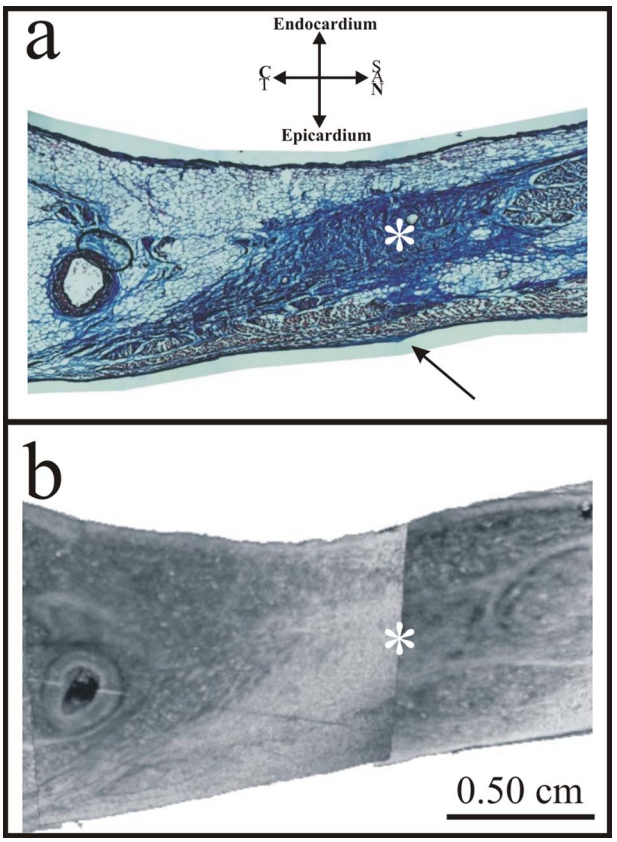

Fig. 7 Transmural OCT of the SAN. (a) Histologic section of the SAN and surrounding tissues. (b) Transmural OCT of the same area. The asterisk (*) identifies the SAN, and the black arrow in (a) points to a thin layer of epicardial fibrous tissue that may have prevented OCT imaging of the SAN from the epicardium. Abbreviations—CT: crista terminalis; SAN: sinoatrial node.

We also imaged the SAN specimen transmurally (i.e., in dissected tissue), which allowed us to consistently locate the SAN throughout its entire length and its proximity to the SAN artery. In this way, we were also able to compare the OCT image to a sister histology section. Due to the prominence of fibroblasts and connective tissue, which serve to isolate the SAN myocytes from the surrounding atrial tissue,[31] the SAN is readily identifiable as a unique structure with transmural OCT (Fig. 7), without the need for histological staining.

3.3 *OCT of the AVJ*

OCT of the AVJ was achieved endocardially in five of nine preparations (56%). In the five preparations whose AVJ was imaged, those junctional elements, including the His bundle and AVN, were located within 2 mm of the endocardial surface. As the average depth penetration in this region across all

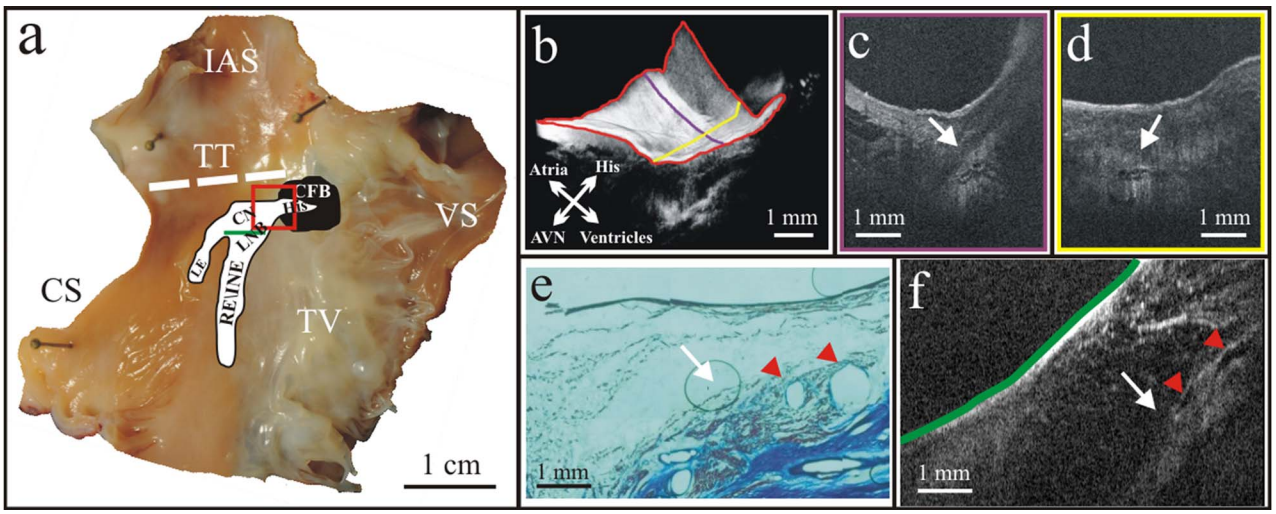

Fig. 8 Endocardial OCT of the AVJ. (a) Dissected AVJ preparation. (b) 3-D reconstruction of the tissue area as indicated by the red box. (c) and (d) 2-D tomograms from (b) as indicated by the purple and yellow lines. (e) Histology of the AVN as indicated by the green line on (a). (f) Corresponding 2-D OCT image of (e) showing a strong relationship between the AV node as defined histologically and via OCT. Red arrowheads indicate blood vessels within the node, visible with both histology and OCT. Abbreviations—IAS: interatrial septum; TT: tendon of Todaro; CS: coronary sinus; LE: leftward extension; CN: compact node; LNB: lower nodal bundle; CFB: central fibrous body; RE: rightward extension; INE: inferior nodal extension; VS: ventricular septum; TV: tricuspid valve; AVN: atrioventricular node. (Color online only.)

specimens was 0.96 ± 0.25 mm, those elements located deeper than 2 mm, as confirmed via histology, were unable to be imaged in this manner.

All AVJ specimens were dissected for imaging of the entire Triangle of Koch, including a 1 to 2-cm border incorporating additional atrial and ventricular tissues [Fig. 8(a)]. The specimens were then optically mapped in overlapping 4.5×4.5 mm segments, with higher resolution images acquired in regions of interest, particularly the His bundle and atrioventricular node (AVN). In Fig. 8, 3-D reconstructions revealed discrete structures located approximately 1 mm below the tissue surface [Fig. 8(b)], corresponding to the locations of the His bundle and AVN as identified with traditional histology. In addition, 2-D tomograms showed this discrete structure encased in fibrous tissue, which manifests as a black envelope surrounding the brighter tissue of the bundle itself [Figs. 8(c) and 8(d)]. As our field of view progresses proximal to the His bundle, approaching the rightward extension (RE), also known as the inferior nodal extension (INE), we have a clear view of the AVN/RE [Figs. 8(e) and 8(f)]. The clarity is such that we can resolve the blood vessels (ranging from 320 to 750 μm in diameter) located within the AVN itself. The blood vessels are identified due to their consistent locations as identified with both histology and OCT.

4 Discussion

Since its inception, OCT has undergone technical advances, including, but not limited to, the establishment of ultrahigh-resolution OCT,[32,33] spectral/Fourier domain OCT,[34–38] numerous improvements in light sources,[39–41] development of a catheter-based imaging probe,[20,21] and ultrasound-enhanced OCT, delivering greater spatial resolution and greater depth penetration.[24,25] However, as OCT technology continues to advance, there still exist technical challenges that remain to be addressed, such as the removal of blood from the imaging field to avoid substantial signal attenuation due to a refractive index mismatch between the cytoplasm of red blood cells (RBCs) and blood plasma. Current intravascular OCT systems incorporate a balloon catheter occlusion system;[8] however, this technique cannot be easily applied to imaging the intact heart. In addition, Dextran, a biocompatible agent, has been shown to substantially improve the resolution and depth of OCT imaging through blood by increasing the refractive index of plasma to a value near that of the RBC cytoplasm.[42,43] This technique, known as index matching, has been shown to significantly diminish signal attenuation; however, additional *in vivo* testing is necessary.

The use of OCT to image the cardiac conduction system and other structures in the intact heart has many potential applications in cardiology. For example, cardiac fibers in the trabeculated endocardial structures of the atria and ventricles, as well as surviving fibers in the infarct border zone, often may contribute to the propensity to develop reentrant arrhythmias.[44,45] Our data indicates that OCT may prove of value in identifying these structures (Figs. 2, 3, and 5), and thus potentially arrhythmic areas of the heart.

Although OCT catheters, with diameters as small as 0.3 mm, are commercially available for intravascular imaging of vulnerable plaques,[8] the size of the target artery and/or tortuosity of the approach may preclude imaging in this manner. In a recent review of the clinical use of intravascular OCT, Guagliumi and Sirbu[8] state that cardiac vessels suitable for intravascular OCT are between 2.5 and 3.75 mm in diameter and have tortuosity angles less than 90 deg.[8] However, for vessels not exhibiting these characteristics, epicardial imaging may be a viable alternative to intravascular imaging (Figs. 3 and 4).

We have also demonstrated OCT imaging of the conduction system, specifically the SAN and AVJ. These components are vital in the normal function of the heart; therefore, the

ability to target them with a high-resolution imaging modality, such as OCT, has any number of potential applications. As the precise location of both the SAN and AVJ within the atrial myocardium is difficult to pinpoint with currently used imaging modalities, their structure can be uniquely identified due to the varying absorption properties present both in the nodal structures, which contain a prominence of fibroblasts and connective tissue, and in the surrounding tissues, as is shown in Figs. 6–8, using OCT.

5 Conclusion

Although traditional cardiac imaging modalities, including MRI, CT, and ultrasound, continue to provide physicians with vital information in the diagnosis of cardiac conditions, we have shown the potential of OCT in providing high-resolution, *in situ* images of the cardiac conduction system and other structures in the intact, explanted human heart. However, despite its ability to distinguish cardiac microstructures as shown in this study, the technique is currently hampered by its limited depth penetration in cardiac tissues. Based on the presented data, we conclude that OCT is emerging as an important imaging modality with the potential to facilitate and guide electrophysiology studies, ablation therapy, implantation of pacing leads, and future cell and tissue engineering therapies subsequent to additional development.

Acknowledgments

The authors would like to thank Paul Iaizzo (University of Minnesota) for contribution of the sinoatrial node specimen. The authors would also like to acknowledge the following funding sources: NIH R01 HL67322 and AHA Grant-in-Aid (IRE) and NIH DA022871 (CMA).

References

1. D. Huang, E. A. Swanson, C. P. Lin, J. S. Schuman, W. G. Stinson, W. Chang, M. R. Hee, T. Flotte, K. Gregory, C. A. Puliafito, and J. G. Fujimito, "Optical coherence tomography," *Science* **254**(5035), 1178–1181 (1991).
2. R. A. Costa, M. Skaf, L. A. Melo Jr., D. Calucci, J. A. Cardillo, J. C. Castro, D. Huang, and M. Wojtkowski, "Retinal assessment using optical coherence tomography," *Prog. Retin Eye Res.* **25**(3), 325–353 (2006).
3. R. Chang and D. L. Budenz, "New developments in optical coherence tomography for glaucoma," *Curr. Opin. Ophthalmol.* **19**(2), 127–135 (2008).
4. W. Drexler and J. G. Fujimoto, "State-of-the-art retinal optical coherence tomography," *Prog. Retin Eye Res.* **27**(1), 45–88 (2008).
5. T. L. Pinto and R. Waksman, "Clinical applications of optical coherence tomography," *J. Interv. Cardiol.* **19**(6), 566–573 (2006).
6. G. J. Tearney, I. K. Jang, and B. E. Bouma, "Optical coherence tomography for imaging the vulnerable plaque," *J. Biomed. Opt.* **11**(2), 021002 (2006).
7. M. E. Brezinski, "Applications of optical coherence tomography to cardiac and musculoskeletal diseases: bench to bedside?" *J. Biomed. Opt.* **12**(5), 051705 (2007).
8. G. Guagliumi and V. Sirbu, "Optical coherence tomography: high resolution intravascular imaging to evaluate vascular healing after coronary stenting," *Catheter Cardiovasc. Interv.* **72**(2), 237–247 (2008).
9. J. Welzel, "Optical coherence tomography in dermatology: a review," *Skin Res. Technol.* **7**(1), 1–9 (2001).
10. T. Gambichler, G. Moussa, M. Sand, D. Sand, P. Altmeyer, and K. Hoffmann, "Applications of optical coherence tomography in dermatology," *J. Dermatol. Sci.* **40**(2), 85–94 (2005).
11. W. Luo, D. L. Marks, T. S. Ralston, and S. A. Boppart, "Three-dimensional optical coherence tomography of the embryonic murine cardiovascular system," *J. Biomed. Opt.* **11**(2), 021014 (2006).
12. M. W. Jenkins, O. Q. Chughtai, A. N. Basavanhally, M. Watanabe, and A. M. Rollins, "*In vivo* gated 4-D imaging of the embryonic heart using optical coherence tomography," *J. Biomed. Opt.* **12**(3), 030505 (2007).
13. B. A. Filas, I. R. Efimov, and L. A. Taber, "Optical coherence tomography as a tool for measuring morphogenetic deformation of the looping heart," *Anat. Rec.* **290**(9), 1057–1068 (2007).
14. M. Gupta, A. M. Rollins, J. A. Izatt, and I. R. Efimov, "Imaging of the atrioventricular node using optical coherence tomography," *J. Cardiovasc. Electrophysiol.* **13**(1), 95 (2002).
15. M. Jenkins, R. S. Wade, Y. Cheng, A. M. Rollins, and I. R. Efimov, "Optical coherence tomography imaging of the purkinje network," *J. Cardiovasc. Electrophysiol.* **16**(5), 559–560 (2005).
16. W. J. Hucker, C. M. Ripplinger, C. P. Fleming, V. V. Fedorov, A. M. Rollins, and I. R. Efimov, "Bimodal biophotonic imaging of the structure-function relationship in cardiac tissue," *J. Biomed. Opt.* **13**(5), 054012 (2008).
17. C. P. Fleming, C. M. Ripplinger, B. Webb, I. R. Efimov, and A. M. Rollins, "Quantification of cardiac fiber orientation using optical coherence tomography," *J. Biomed. Opt.* **13**(3), 030505 (2008).
18. B. Povazay, K. Bizheva, A. Unterhuber, B. Hermann, H. Sattmann, A. F. Fercher, W. Drexler, A. Apolonski, W. J. Wadsworth, J. C. Knight, P. S. Russell, M. Vetterlein, and E. Scherzer, "Submicrometer axial resolution optical coherence tomography," *Opt. Lett.* **27**(20), 1800–1802 (2002).
19. J. G. Fujimoto, "Optical coherence tomography for ultrahigh resolution *in vivo* imaging," *Nat. Biotechnol.* **21**(11), 1361–1367 (2003).
20. G. J. Tearney, M. E. Brezinski, S. A. Boppart, B. E. Bouma, N. Weissman, J. F. Southern, E. A. Swanson, and J. G. Fujimoto, "Images in cardiovascular medicine. Catheter-based optical imaging of a human coronary artery," *Circulation* **94**(11), 3013 (1996).
21. G. J. Tearney, M. E. Brezinski, B. E. Bouma, S. A. Boppart, C. Pitris, J. F. Southern, and J. G. Fujimoto, "*In vivo* endoscopic optical biopsy with optical coherence tomography," *Science* **276**(5321), 2037–2039 (1997).
22. Z. Chen, T. E. Milner, S. Srinivas, X. Wang, A. Malekafzali, M. J. van Gemert, and J. S. Nelson, "Noninvasive imaging of *in vivo* blood flow velocity using optical Doppler tomography," *Opt. Lett.* **22**(14), 1119–1121 (1997).
23. A. M. Rollins, S. Yazdanfar, J. K. Barton, and J. A. Izatt, "Real-time *in vivo* color Doppler optical coherence tomography," *J. Biomed. Opt.* **7**(1), 123–129 (2002).
24. J. O. Schenk and M. E. Brezinski, "Ultrasound induced improvement in optical coherence tomography (OCT) resolution," *Proc. Natl. Acad. Sci. U.S.A.* **99**(15), 9761–9764 (2002).
25. C. Huang, B. Liu, and M. E. Brezinski, "Ultrasound-enhanced optical coherence tomography: improved penetration and resolution," *J. Opt. Soc. Am. A* **25**(4), 938–946 (2008).
26. M. E. Brezinski, *Optical Coherence Tomography: Principles and Applications*, Elsevier, New York (2006).
27. Z. Hu and A. M. Rollins, "Quasi-telecentric optical design of a microscope-compatible OCT scanner," *Opt. Express* **13**(17), 6407–6415 (2005).
28. G. J. Tearney, H. Yabushita, S. L. Houser, H. T. Aretz, I. K. Jang, K. H. Schlendorf, C. R. Kauffman, M. Shishkov, E. F. Halpern, and B. E. Bouma, "Quantification of macrophage content in atherosclerotic plaques by optical coherence tomography," *Circulation* **107**(1), 113–119 (2003).
29. S. Y. Ho, R. H. Anderson, and D. Sanchez-Quintana, "Atrial structure and fibers: morphologic bases of atrial conduction," *Cardiovasc. Res.* **54**(2), 325–336 (2002).
30. M. E. Brezinski, G. J. Tearney, B. E. Bouma, J. A. Izatt, M. R. Hee, E. A. Swanson, J. F. Southern, and J. G. Fujimoto, "Optical coherence tomography for optical biopsy. Properties and demonstration of vascular pathology," *Circulation* **93**(6), 1206–1213 (1996).
31. M. R. Boyett, H. Honjo, and I. Kodama, "The sinoatrial node, a heterogeneous pacemaker structure," *Cardiovasc. Res.* **47**(4), 658–687 (2000).
32. W. Drexler, U. Morgner, F. X. Kartner, C. Pitris, S. A. Boppart, X. D. Li, E. P. Ippen, and J. G. Fujimoto, "*In vivo* ultrahigh-resolution optical coherence tomography," *Opt. Lett.* **24**(17), 1221–1223 (1999).
33. W. Drexler, "Ultrahigh-resolution optical coherence tomography," *J. Biomed. Opt.* **9**(1), 47–74 (2004).
34. A. F. Fercher, C. K. Hitzenberger, G. Kamp, and S. Y. El-Zaiat,

"Measurement of intraocular distances by backscattering spectral interferometry," *Opt. Commun.* **117**, 43–48 (1995).
35. M. Wojtkowski, R. Leitgeb, A. Kowalczyk, T. Bajraszewski, and A. F. Fercher, "*In vivo* human retinal imaging by Fourier domain optical coherence tomography," *J. Biomed. Opt.* **7**(3), 457–463 (2002).
36. S. H. Yun, G. J. Tearney, J. F. de Boer, N. Iftimia, and B. E. Bouma, "High-speed optical frequency-domain imaging," *Opt. Express* **11**(22), 2953–2963 (2003).
37. N. Nassif, B. Cense, B. H. Park, S. H. Yun, T. C. Chen, B. E. Bouma, G. J. Tearney, and J. F. de Boer, "*In vivo* human retinal imaging by ultrahigh-speed spectral domain optical coherence tomography," *Opt. Lett.* **29**(5), 480–482 (2004).
38. W. Y. Oh, S. H. Yun, B. J. Vakoc, M. Shishkov, A. E. Desjardins, B. H. Park, J. F. de Boer, G. J. Tearney, and B. E. Bouma, "High-speed polarization sensitive optical frequency domain imaging with frequency multiplexing," *Opt. Express* **16**(2), 1096–1103 (2008).
39. B. E. Bouma, G. J. Tearney, S. A. Boppart, M. R. Hee, M. E. Brezinski, and J. G. Fujimoto, "High-resolution optical coherence tomographic imaging using a mode-locked Ti:Al2O3 laser source," *Opt. Lett.* **20**(13), 1486–1488 (1995).
40. B. E. Bouma, G. J. Tearney, I. P. Bilinsky, B. Golubovic, and J. G. Fujimoto, "Self-phase-modulated Kerr-lens mode-locked Cr:forsterite laser source for optical coherence tomography," *Opt. Lett.* **21**(22), 1839–1841 (1996).
41. A. Unterhuber, B. Povazay, K. Bizheva, B. Hermann, H. Sattmann, A. Stingl, T. Le, M. Seefeld, R. Menzel, M. Preusser, H. Budka, C. Schubert, H. Reitsamer, P. K. Ahnelt, J. E. Morgan, A. Cowey, and W. Drexler, "Advances in broad bandwidth light sources for ultrahigh resolution optical coherence tomography," *Phys. Med. Biol.* **49**(7), 1235–1246 (2004).
42. M. Brezinski, K. Saunders, C. Jesser, X. Li, and J. Fujimoto, "Index matching to improve optical coherence tomography imaging through blood," *Circulation* **103**(15), 1999–2003 (2001).
43. X. Xu, L. Yu, and Z. Chen, "Optical clearing of flowing blood using dextrans with spectral domain optical coherence tomography," *J. Biomed. Opt.* **13**(2), 021107 (2008).
44. M. Valderrabano, M. H. Lee, T. Ohara, A. C. Lai, M. C. Fishbein, S. F. Lin, H. S. Karagueuzian, and P. S. Chen, "Dynamics of intramural and transmural reentry during ventricular fibrillation in isolated swine ventricles," *Circ. Res.* **88**(8), 839–848 (2001).
45. M. Valderrabano, "Influence of anisotropic conduction properties in the propagation of the cardiac action potential," *Prog. Biophys. Mol. Biol.* **94**(1–2), 144–168 (2007).